

# Wind turbine performance in natural icing environments: A field characterization

Linyue Gao<sup>a</sup>, Jiarong Hong<sup>a,b,\*</sup>

<sup>a</sup> St. Anthony Falls Laboratory, University of Minnesota, Minneapolis, MN 55414, USA

<sup>b</sup> Department of Mechanical Engineering, University of Minnesota, Minneapolis, MN 55455, USA

## ARTICLE INFO

### Keywords:

Wind turbine icing  
Structural response  
Power loss  
Performance degradation  
Field measurement  
Natural icing environment

## ABSTRACT

Over 30% worldwide installations of wind turbines in cold climate regions are threatened with icing risks. The current study presents a systematic characterization of the turbine operation, power production, and blade/tower structural responses of a utility-scale wind turbine (2.5 MW, variable-speed variable-pitch regulated) under natural icing environments, by leveraging the unique facilities at the Eolos Wind Energy Research Field Station. A representative icing event that lasts 51 h is selected and divided into pre-icing, operational-icing, stopped-icing, and post-icing phases based on the variation of turbine operational conditions (i.e., power, rotor speed, and pitch angle) for the detailed evaluation. The results show that ice accretion can lead to appreciable reductions in the rotor speed and pitch angle before the turbine reaches its operational limits. Such reductions increase correspondingly as the inflow wind speed increases, which may accelerate the airfoil stall process and result in more severe power loss. The 51-h icing event yields a total energy loss of ~25 MWh, and the post-icing phase contributes a second-largest share of 17%, on the heel of the stopped-icing phase of 71%, associated with the long duration of natural ice melting process. Besides, blade structural response is highly sensitive to the ice accretion due to its fast reaction to the ice-induced lift penalties. The tower response also provides concrete evidence for the increase of the structural imbalance with ice accretion. Our findings can provide insights into the development of advanced control strategies for a more efficient and safer operation of wind turbines in natural icing environments.

## 1. Introduction

Over 30% of worldwide installations of wind turbines in cold climate regions are threatened with ice accretion on turbine structures (Lehtomäki, 2016). Such ice accretion can lead to a substantial reduction of turbine power generation (Homola et al., 2012b; Lamraoui et al., 2014; Ribeiro and Beckford, 2016; Blasco et al., 2017a; Zanon et al., 2018), increase in structural loading (Barker et al., 2005; Gravesen et al., 2005; Alsabagh et al., 2013;) and even cause safety issues through ice shedding from rotating turbine blades (Morgan et al., 1998). In particular, ice accretion can drastically alter the turbine blade profile, and induce severe aerodynamic penalties, i.e., lift decrease and drag increase, leading to up to 50% annual production losses (Fakorede et al., 2016). The unevenly distributed ice structures can add additional loads and edge-wise vibration to the turbine and cause imbalance to the rotating system (Shi et al., 2016; Hu et al., 2017), which in the long term may shorten the life-span of wind turbines.

So far, the majority of studies of the ice-induced effect on wind turbines are conducted via numerical simulations (Homola et al., 2012a, 2012b; Etemaddar et al., 2014; Pedersen and Sørensen, 2016; Yirtici et al., 2016; Hu et al., 2017). Up to now, the simulations for the full-size wind turbines with detailed blade configurations are not affordable, let alone solving the fields near the tiny ice roughness. As a solution, the iced profiles for 2D airfoils or semi-3D blade sections are modeled first with ice accretion codes, such as LEWICE (Jasinski et al., 1997), FENSAP-ICE (Makkonen et al., 2001; Beaugendre et al., 2003; Reid et al., 2013; Son et al., 2019), and TURBICE (Laakso et al., 2005; Homola et al., 2010). The aerodynamic properties of the iced profiles, i.e., lift and drag coefficients, are then estimated via CFD simulations (Bragg et al., 2005; Molina et al., 2018; Tagawa et al., 2018; Gantasala et al., 2019). The lift and drag acting on the blade sections are further integrated to turbine power information by implementing the blade element momentum (BEM) theory (Homola et al., 2012a, 2012b; Etemaddar et al., 2014). Following the power analysis, the structural responses can be estimated

\* Corresponding author at: St. Anthony Falls Laboratory, University of Minnesota, Minneapolis, MN 55414, USA.

E-mail address: [jhong@umn.edu](mailto:jhong@umn.edu) (J. Hong).

<https://doi.org/10.1016/j.coldregions.2020.103193>

Received 6 April 2020; Received in revised form 8 September 2020; Accepted 15 October 2020

Available online 18 October 2020

0165-232X/© 2020 Elsevier B.V. All rights reserved.

by using aero-elastic codes, such as HAWC2 (Etemaddar et al., 2014; Shi et al., 2016) and FAST (Hu et al., 2017; Gantasala et al., 2019). Etemaddar et al. (2014) provided the first comprehensive assessment of the ice-induced power reduction and structural degradation on the simulated NREL 5 MW turbine. Their study showed an overall power loss of up to 35% and a shift of the rated power from a wind speed of 11 m/s to 19 m/s similar to that reported by Homola et al. (2012a, 2012b). In addition, they also observed the blade flapwise moment decreases due to icing below the rated wind speed but increases above it. Through a simulation of a two-bladed NREL Phase VI turbine at a fix wind speed of 8 m/s under different blade ice accretion conditions (i.e., icing on only one and both blades), Hu et al. (2017) found that the blade moments decrease under both conditions while the tower side-to-side moment increases with icing on one blade and reduces with icing on both blades. Despite the vigorous simulation effort of turbine icing, there is still a significant gap between the settings used in the simulation and those associated with turbine icing in the field, even for the state-of-the-art simulations. The current simulations use primarily 2D modeling of ice accretion and the associated aerodynamic penalties, neglecting important 3D flow and turbulent effect on the estimation of lift and drag. Even with such simplified modeling, the computational cost is still too high to provide the time-resolved power and structural response during the turbine icing process.

Currently, most experiments for validating turbine icing simulations are conducted with model-scale turbines under controlled icing conditions in the laboratory. Using the Icing Research Tunnel at Iowa State University (ISU-IRT), Gao et al. (2019b, 2019c, 2020a) conducted a series of experiments to obtain 3D ice accretion profiles on blade sections and corresponding aerodynamic penalties, which can be incorporated into BEM models for estimating the energy loss of turbines operating under icing conditions (Blasco et al., 2017a). By placing a 100 W model turbine in a 7.8 m × 11.6 m artificial climate chamber, Shu et al. (2017) provided a systematic characterization of the change of turbine load power, rotor speed, and shaft torque during a 8-min icing process. Their results showed the load power and rotor speed have a 90% decline within the first 4 min while the shaft torque rises slightly within the first 2 min and then falls rapidly. In addition to turbine operation, the laboratory studies of turbine structural response under icing conditions are mainly concentrated on offshore turbine foundations (Barker et al., 2005; Gravesen et al., 2005; Hendrikse et al., 2018) with conditions deviating from those of inland turbines. Despite the past and ongoing efforts, both turbine (e.g., model scalability, turbine control strategies, etc.) and environment conditions (e.g., turbulence and atmospheric stability) in these laboratory tests differ substantially from those for the turbines operating in the field. Therefore, to provide an ultimate assessment of these numerical and laboratory icing studies and improve their applicability for turbine icing in practice, it is highly desirable to conduct detailed characterization of the turbine operation and structural response under realistic icing conditions in the field.

Unfortunately, such information is quite scarce in the literature primarily due to the lack of publicly-accessible data of turbine operation from wind farm owners and the well-instrumented utility-scale turbine with sensors providing high-resolution monitoring of their structural response. Up to now, nearly all of the field measurements in the published literature are focused on examining the ice-induced power reduction with the data from the standard Supervisory Control and Data Acquisition (SCADA) system (René et al., 2009; Davis et al., 2016b; Shu et al., 2018; Gao, 2019; Roberge et al., 2019). Specifically, René et al. (2009) indicated that ice detection via power curve seems to work considerably well except for light icing and during periods with low wind speed based on their observations in the midst of the Swiss Alps. With field observation confirming the ice accretion on turbine blades, Shu et al. (2018) and Gao (2019) showed that ice accretion at the leading edge of blade tip with thickness around 20% of local chord length can lead to more than 80% power reduction for 300 kW and 1.5 MW turbines, respectively. They also provided field evidence of the

rotor speed reduction with the increase of icing load, which can be implemented for turbine icing detection. In addition, Roberge et al. (2019) presented that most of the icing events (e.g., freezing rain and in-cloud icing) occur between  $-10^{\circ}\text{C}$  to  $0^{\circ}\text{C}$  with a relative humidity (RH) level higher 85% based on 2-year field observations in eastern Canada, suggesting that meteorological icing conditions can also be used for turbine icing detection.

Consequently, the present study aims to address aforementioned limitations in literature and provide a better understanding of how a utility-scale wind turbine behaves in the course of a natural icing process. Specifically, we seek to provide comprehensive information about the variation of turbine operation, icing-induced power reduction as well as the structural response of a utility-scale turbine in the entire course of a natural icing process in the field. Our study demarcates the turbine icing process into multiple phases based on distinct characteristics of turbine operation and identifies valuable features of turbine structural (both blade and tower) responses for each phase. Such information can be potentially incorporated into advanced turbine control strategies for improving turbine efficiency and mitigating the impact of icing in cold climate regions. The current study is conducted by leveraging the unique facilities available at the Eolos Wind Energy Research Field Station, including a 2.5 MW wind turbine instrumented with blade and tower strain sensors and a meteorological tower for characterizing local flow conditions. A representative icing event is selected using the method described in Section 2. Such an icing event is divided into four phases based on the variation of turbine operation during the event in Section 3 with the follow-up analysis on ice-induced power reduction and blade and tower structural response for each phase provided in the same section. Section 4 summarizes our findings and discusses their implications on advanced turbine control strategies for icing mitigation.

## 2. Methodology

### 2.1. Experimental facility and database

The study is conducted using the database from the Eolos station at the University of Minnesota in Rosemount, MN, USA (<http://eolos.umn.edu/data-collection>). As shown in Fig. 1(a), the station hosts a 2.5 MW upwind three-bladed horizontal-axis wind turbine (Clipper Liberty, C96) and a 130 m meteorological tower 170 m south to the turbine (referred to as met tower hereafter). This turbine is variable-speed variable-pitch (VSVP) regulated. The rotor diameter ( $D$ ) and hub height ( $H$ ) are 96 m and 80 m, respectively. The cut-in, rated, and cut-out wind speeds at hub height are  $\sim 4$  m/s, 11 m/s, and 25 m/s, respectively. The turbine adopts different control strategies in three regions partitioned with the aforementioned three wind speeds, as shown in Fig. 1(d). In Region 1 (i.e.,  $U_{\text{hub}} < 4$  m/s), the turbine has no power generation. In Region 1.5 (i.e.,  $4$  m/s  $\leq U_{\text{hub}} \leq 6.9$  m/s), Region 2 (i.e.,  $6.9$  m/s  $\leq U_{\text{hub}} \leq 9.2$  m/s), and Region 2.5 (i.e.,  $9.2$  m/s  $\leq U_{\text{hub}} \leq 11$  m/s), the turbine is generator torque-controlled with increasing rotor speed as the inflow wind speed increases. Region 2 refers to the most efficient turbine operational conditions with the maximum power coefficient ( $C_{p,\text{max}}$ ) of 0.472. Region 1.5 and Region 2.5 correspond to the transitions between Region 2 and its neighbors. In Region 3 (i.e.,  $U_{\text{hub}} > 11$  m/s), the turbine is full-span collective-pitch regulated to achieve stable rated power output. According to historical data at the Eolos station, the turbine has a high probability of operating in Region 1.5–2.5 (>70%) than Region 3 (<5%) and Region 1 ( $\sim 20\%$ ). The SCADA system records the turbine operational conditions at a sampling rate of 1 Hz. In addition, the turbine is instrumented with blade and tower sensor systems to measure the real-time structural response at a sampling rate of 20 Hz. All three blades are instrumented with the same setup of the blade sensors. For each blade, the blade sensor system consists of four groups of fiberoptic strain gauges (Micron Optics, os3200) installed at the different radial positions along the blade, i.e., blade root (RT), 25% R ( $r_2 = 10.7$  m), 37.5% R ( $r_3$

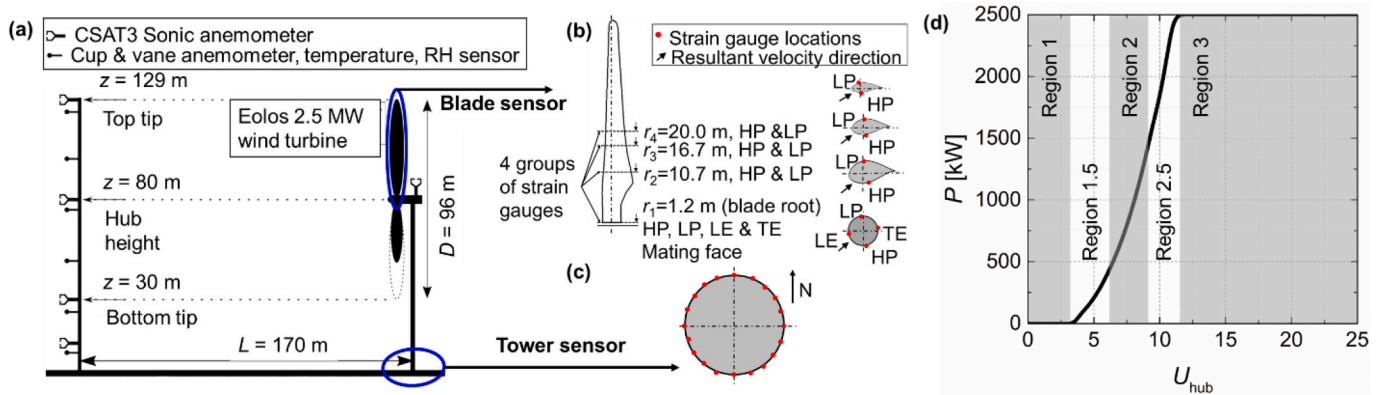


Fig. 1. Schematics of (a) the 2.5 MW wind turbine and the met tower at the Eolos station, (b) the blade strain gauges installed at the blade root, (c) the tower sensor system with 20 strain gauges installed at the tower base, and (d) power curve of the wind turbine.

= 16.7 m), and 45%  $R$  ( $r_4 = 20.0$  m), where  $R$  is the radius of the turbine rotor. Four strain gauges are installed over the high-pressure (HP) side surface, low-pressure (LP) side surface, leading-edge (LE) region, and trailing-edge (TE) region of the cross-section at the blade root, i.e., 1.2 m from the mating face, as shown in Fig. 1(b). Six strain gauges are mounted over the HP and LP surfaces of the cross-sections at other outer radial positions. The tower sensor system consists of 20 single-axis strain gauges (Vishay MicroMeasurements, CEA-06-125UN-350/P2) evenly distributed around the tower base, as shown in Fig. 1(c). Note that the working temperature for each strain gauge is simultaneously measured to compensate for the temperature effect on the strain measurement. More detailed information on the turbine blade and tower sensor systems are available in the previous publications using the Eolos database (Chamorro et al., 2015b; Gao et al., 2020b).

The met tower is mounted with velocity, temperature, and relative humidity (RH) sensors at multiple elevations to characterize local meteorological conditions. As shown in Fig. 1(a), the sonic anemometers (Campbell Scientific, CSAT3) with a sampling rate of 20 Hz are installed at four elevations, i.e., 10 m, 30 m, 80 m, and 130 m, the latter three of which correspond to the turbine bottom blade tip, hub height and top blade tip, respectively. The cup & vane anemometers (Met One, 014-A) and temperature and RH sensors (Met One, 083-E) with a sampling rate of 1 Hz are installed at six elevations, four of which correspond to elevations three meters below those of sonic anemometers, i.e., 7 m, 27 m, 77 m, and 127 m. Two other elevations are 52 m and 102 m, which match the mid-spans of lower and upper blades, respectively.

## 2.2. The selection of icing event

According to the ice classification standard from the International Energy Agency (IEA) (Lehtomäki, 2016), the Eolos station belongs to the IEA Ice class II site. Observations of turbine icing events have been reported from late October to early April at the station since its service started in 2011. Therefore, the nine-year Eolos database provides us opportunities to identify turbine icing events under standard meteorological icing conditions. For the present study, the icing event is selected using the following criteria. First, the ambient air temperature ( $T$ ) is set to be lower than  $3^\circ\text{C}$  (Ihliis, 2015), and RH is set to be higher than  $\text{RH} > 85\%$  (Shu et al., 2018) to meet the meteorological icing conditions which are the prerequisite of turbine icing. It should be noted that RH-based criterion is commonly used in the field studies (Shu et al., 2018) to present the combined effect of the liquid water content (LWC) level and medium volumetric diameter (MVD) that used in laboratory studies (Gao et al., 2019a, 2019c, 2020a) for identifying icing conditions. Second, the reduction of the power of 15% with respect to that produced under no-icing conditions is used as a threshold to detect icing events according to the literature (Davis, 2014; Lamraoui et al., 2014; Davis

et al., 2016a; Davis et al., 2016b; Hansson et al., 2016; Zhang et al., 2018). The power reduction is defined as the difference between the measured power production (denoted as  $P_{\text{mea}}$  hereafter) and corresponding power production under no icing conditions (denoted as  $P_{\text{no-icing}}$  hereafter) modeled based on the real-time  $U_{\text{hub}}$  and the turbine ideal power curve with an eighth-order polynomial fit. Note that the power reduction due to other factors, such as the power grid curtailment and turbine overheating issues, are excluded here based on the real-time power limit information. Third, considering the instrument glitches under field icing conditions (e.g., signal loss, met anemometer measurement failure, etc.), we only select the icing events with more than 95% of the time that all the instruments including the met tower, the turbine SCADA system, blade, and tower sensor systems are in normal operating conditions to ensure sufficient data for further analysis.

Based on the criteria mentioned above, we examined the database using a sliding window approach with a window size of 1 h and an advancing increment of 10 min to obtain all the candidate time periods of 1 h. The candidate time periods adjacent in time are then combined to yield the time period of an icing event. Such a sliding window method has been widely used for data selection from the Eolos database (Chamorro et al., 2015a; Chamorro et al., 2015b; Gao et al., 2020b). Note that for each identified icing event, we also expanded it backward in time to include the period when the meteorological icing conditions are met, but no power reduction is observed, and forward in time to include the time period that the turbine fully returns to its normal operation. Icing events with further confirmation according to the field observations of blade icing or icing fault log are topped in the selection, as recommended by Battisti (2015). Finally, an icing event that lasts 51 h in the period of 2018-02-19 8:00:00.000 to 2018-02-21 10:59:59.950 UTC was selected for the present study. Fig. 2(a) and (b) presents the time series of the meteorology conditions, i.e.,  $T$ , RH,  $U_{\text{hub}}$  and wind direction ( $\theta$ ), during this icing event confirmed further by the photo of turbine blade icing captured with a camera on the ground shown in Fig. 2(c). This event has a good correlation with the precipitation (snow) record, suggesting being a precipitation-icing event. The white appearance and tiny structures of the ice accreted over the blade surfaces, as well as the information of  $T$  and RH, imply the type of ice might be rime ice or mixed ice. As the figures show, the meteorological conditions are largely stationary in the selected icing event, except for a drop of  $T$  and RH after  $\sim 33$  h and a drastic change of wind direction of  $\sim 120^\circ$  after 33 h from the beginning of the icing event. It should be noted that the Eolos turbine automatically reorients towards the inflow winds via the adjustment in yaw angle. The averaged yaw error, i.e., the difference between the wind direction and nacelle direction, is small and negligible ( $0.6^\circ$ ).

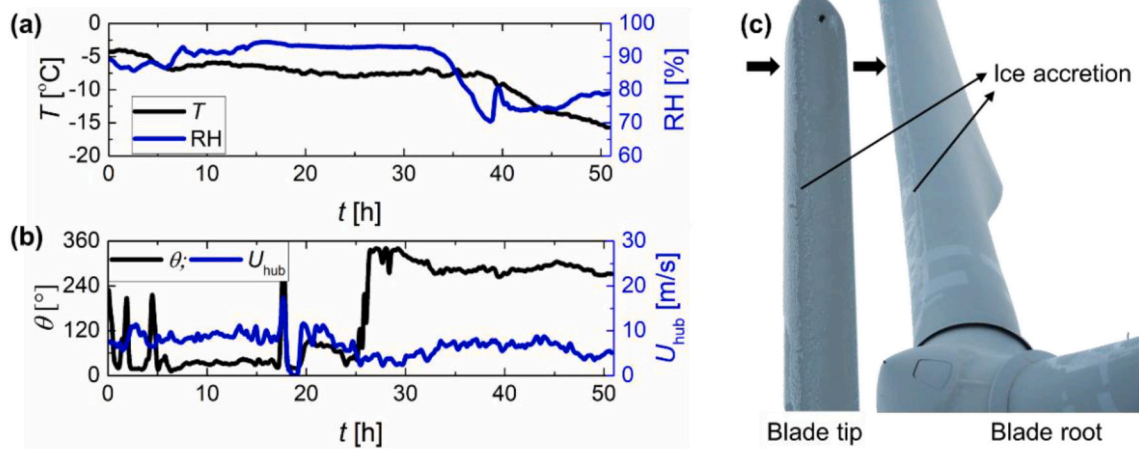


**Fig. 2.** Time series of (a) air temperature ( $T$ ) and relative humidity (RH), and (b) wind speed at hub height ( $U_{hub}$ ) and wind direction ( $\theta$ ) during the selected icing event with 10-min smoothed data. (c) Sample photos of ice accretion on the turbine blade during the selected icing event.

2.3. Icing phase identification

Based on the variation of turbine operational conditions, we first divide an icing event into four phases, i.e., pre-icing, operational-icing, stopped-icing, and post-icing phases as below (illustrated in Fig. 3).

Pre-icing phase: Turbine operation does not exhibit appreciable difference compared with those under no icing conditions even though meteorological icing conditions, i.e.,  $T < 3$  °C and  $RH > 85\%$ , are satisfied according to literature (Fakorede et al., 2016).

- Operational-icing phase: The turbine exhibits an appreciable reduction in power ( $\Delta P > 15\%$ ) and rotor speed due to ice accretion but remains in operation (Shu et al., 2017, 2018; Gao, 2019).
- Stopped-icing phase: The turbine generates no power ( $P = 0$  kW) and stays standstill/idling with blade feathering due to a significant amount of ice accretion on blades.
- Post-icing phase: Turbine starts to generate power ( $P > 0$  kW) until its full recovery to regular operation as the remaining ice is completely removed through naturally melting or shedding/falling

Note that the presence of different icing phases for wind turbines operating under icing conditions was first proposed by Kraj and Bibeau (2010), but their study did not provide any quantitative connection between icing accretion and turbine operational conditions. In addition, the icing phases may not occur strictly in sequential order in practice since the development of ice (i.e., accretion and melting) on a turbine is susceptible to changing meteorological conditions in the field.

3. Results and discussion

3.1. Turbine operational variations

We first investigate the variation of the turbine operational parameters (i.e., power, rotor speed, and blade pitch) during the selected icing event in the present study, as shown in Fig. 4. According to the criteria described above, the event is divided into pre-icing (~6.5 h), operational-icing (~8.5 h), stopped-icing (~24 h), and post-icing (~12 h) phases based on a comparison of the measured and modeled turbine parameters under no-icing conditions with the same inflow wind speed (referred to as “no-icing” data hereafter). As the figure shows, in our selected event, the four icing phases take place generally in sequential order. However, though constituting only 5% of total time duration, an alternation between operational and stopped phases does occur at around 15th hour of the event, as shown in a small surge of the measured power in Fig. 4(a). Noticeably, the overall energy loss of the selected icing event, i.e.,  $\Delta E = \Sigma(P_{no-icing} - P_{mea})\Delta t$ , is approximately 25 MWh, i.e., 63% of the amount of energy to be generated (~40 MWh). For a 0.10 \$/kWh contract, this energy loss is equivalent to a \$ 2511 financial deficit for this event. The four phases mentioned above take account for 0%, 12%, 71%, and 17% of the total energy loss, respectively. The post-icing phase owns an even larger proportion than that of the operational-icing phase mainly due to its longer duration caused by the slow natural melting process.

To conduct further analysis of turbine operation and structural response under different icing phases, five sample datasets of one-

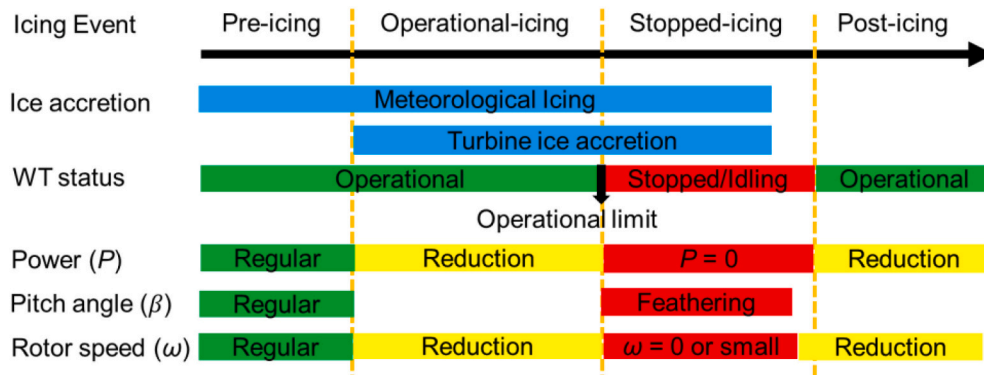


**Fig. 3.** Schematic illustrating the variation of icing and turbine operational conditions during different phases of an icing event, i.e., pre-icing, operational-icing, stopped-icing, and post-icing.

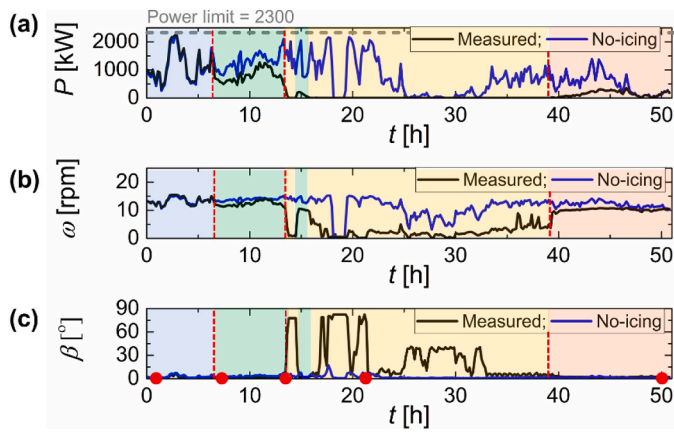


**Fig. 4.** Time series of the measured and no-icing wind turbine quantities in four icing phases during the selected icing event, including (a) power ( $P$ ), (b) rotor speed ( $\omega$ ), and (c) pitch angle ( $\beta$ ), using 10-min smoothed data. Note that the pitch angle here refers to the global pitch angle that has the same value at different radius positions and is commonly used and recorded in the SCADA dataset. The power production under no icing conditions is modeled based on the real-time  $U_{hub}$  and the turbine ideal power curve with an eighth-order polynomial fit. Similar methods are used for the modeling of modeled rotor speed and pitch angle under no icing conditions. Different color bands mark different icing phases. Blue, green, yellow, and red represent pre-icing, operational-icing, stopped-icing, and post-icing phases, respectively. The power limit has a constant value of 2.3 MW during the selected period. Note that the red dots in (c) mark the location of the sample datasets selected from each icing phase for further analysis.

duration each, denoted as P1, P2-I, P2-T, P3, and P4, are selected, as indicated by the red dots in Fig. 4(c). The 1-h duration ensures not only sufficient data but also relatively stable inflow conditions, such as wind speed and wind direction, which allows us to conduct further analysis, especially the spectral analysis for turbine structures in Section 3.3 (Gao et al., 2020b). It should be noted that the third sample dataset (P2-T) corresponds to the transition status between the operational and stopped-icing phases to shed light on the transient turbine behaviors as the turbine reaches its operational limit due to ice accretion. Table 1 summarizes the general meteorological and turbine operational information for each sample dataset. The temperature and RH in all datasets, except P4, satisfy the meteorological icing conditions. The lower temperature and RH in P4 suggests no more ice accretion during this period. The turbine operation follows the conventional control strategy in Region 2, Region 2, Region 2.5, Region 2.5, and Region 1.5 from P1 to P4, respectively. The rotor speed yields a reduction of 1% (P1, negligible), 14% (P2), 63% (P2-T), 88% (P3), and 5% (P4) while apparent increments in blade pitch angle are observed in P2-T and P3.

Fig. 5 presents the time series of the measured and no-icing rotor speed ( $\omega$ ) and pitch angle ( $\beta$ ) for each sample dataset. In P1, the measured and no-icing data for both  $\omega$  and  $\beta$  match very well based on the conventional control strategy of the wind turbine, confirming that there is no appreciable icing effect on turbine operation in the pre-icing phase. The turbine is in its regular operation with a small pitch angle of

$\sim 1^\circ$ . In P2-I, the rotor speed exhibits a reduction of 15% (compared to the no-icing value) after approximately 1.5-h under icing conditions. Accordingly, as shown in the zoomed-in inset in Fig. 5(b), the blade ice accretion in this period also causes a decrease of fluctuations in  $\beta$ , suggesting the turbine under operational icing conditions become less sensitive to inflow changes. During the P2-T, the  $\omega$  and  $\beta$  first show a similar reduction as those in P2-I observed. As soon as the turbine reaches its operational limit due to severe blade ice accretion, a sharp drop in  $\omega$  and a rise in  $\beta$  take place, indicating that the turbine makes a transition to idling mode to reduce the gained aerodynamic forces for safety concerns actively and confirmed with a fault alarm in the SCADA signals. In some circumstances, the sharp drop might be a consequence of the amount of the ice on the blade that would not allow generating enough torque, mainly due to a significant increase in drag. In P3 (i.e., during the stopped-icing phase), the turbine is in a standstill status with almost no blade rotation at the beginning. Later (i.e.,  $\sim 28$  min from the beginning), the turbine is observed to struggle to recover its operation indicated by a nonzero but small  $\omega$ . Such a change of operation is accompanied by a steep drop of  $\beta$ , which is likely to be caused by sudden blade load reduction associated with intermittent shed-off of ice chunks from the blades. This phenomenon is commonly observed in practical turbine operation due to the highly-varying icing conditions in the field (Battisti, 2015). In P4 (i.e., during the post-icing phase), the  $\beta$  quickly returns to its normal operating conditions while the  $\omega$  still stays below its no-icing value, potentially due to the remaining ice structures on turbine blades.

The information above suggests that  $\omega$  and  $\beta$  are useful indicators for ice detection though they have not been used as detection parameters in the literature (Zhang et al., 2018). The reduction in  $\omega$  is positively correlated to the decrease in rotor torque caused by the aerodynamic force changes and increased gravitational and centrifugal forces due to ice accumulation, as shown in Fig. 6(a). This trend confirms that based on the conventional control strategy,  $\omega$  is set to decrease to match the designed generator torque via prefab drivelines for a new stability. This conventional control strategy is suggested to be improved to avoid stops and keep the turbine operating for more power production, such as the “Operation with Ice” (OWI) strategy launched by Siemens Gamesa Renewable Energy, 2019. The lower  $\omega$  is also accompanied by a  $\beta$  response that is less sensitive to the inflow changes. In addition, the reduction in  $\omega$  and  $\beta$  is found to be associated with the magnitude of inflow speed. As shown in Fig. 6(b) and (c), the impact of turbine ice accretion on turbine operation, i.e.,  $\Delta\omega$  and  $\Delta\beta$ , escalates as the inflow speed increases.

### 3.2. Power reduction evaluation

In this section, the ice-induced power reduction is investigated in each icing phase using the dataset presented in the previous section. Fig. 7 shows the time series of the measured and no-icing power generation for the selected sample datasets. In P1, as shown in Fig. 7(a), the measured power output matches closely with that of no-icing power, showing no signs of icing in the pre-icing phase. In P2-I (i.e., after the 1.5-h into the operational-icing phase), as shown in Fig. 7(b), the signal of the measured power follows a similar trend as the no-icing

**Table 1**

Meteorological and turbine operational conditions of the selected 1-h datasets for different icing phases. Note that the information listed in the table is obtained through the 1-h average of measured and no-icing data.

Sample datasets	$T$ [°C]	RH [%]	$U_{hub}/Region$ [m/s]	$\theta$ [°]	$\omega_{mea}$ [rpm]	$\omega_{no-icing}$ [rpm]	$\beta_{mea}$ [°]	$\beta_{no-icing}$ [°]
P1: Pre-icing	-4.2	88	7.1/Region 2	6	12.3	12.5	1	1
P2-I: Operational-icing (Initial)	-6.7	92	7.7/Region 2	26	11.5	13.3	1	2
P2-T: Operational-icing (Transition)	-6.3	92	10.1/Region 2.5	40	5.3	14.5	23	5
P3: Stopped-icing	-7.5	93	10.6/Region 2.5	81	1.5	12.7	42	6
P4: Post-icing	-15.5	79	5.2/Region 1.5	272	10.5	11.0	2	1

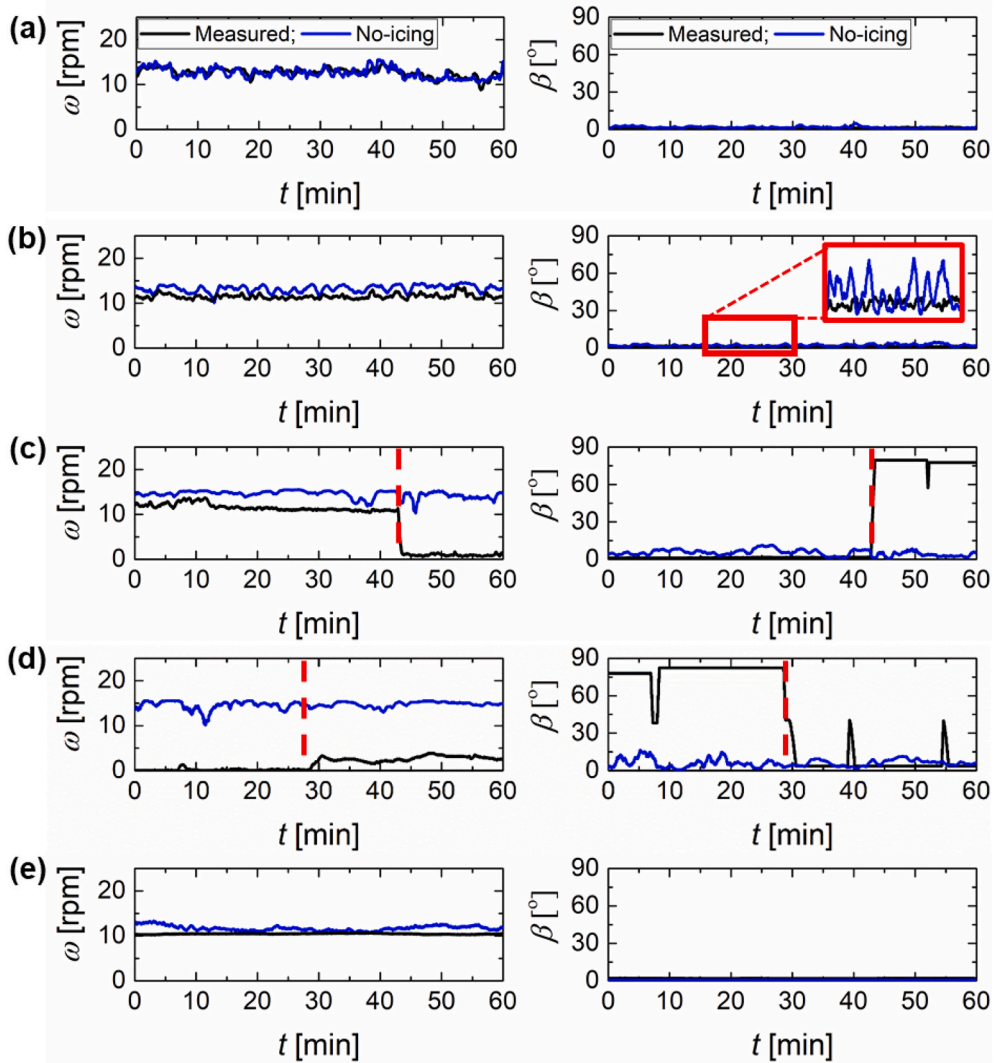


Fig. 5. Time series of the rotor speed ( $\omega$ ) and pitch angle ( $\beta$ ) for (a) P1, (b) P2-I, (c) P2-T, (d) P3, and (e) P4 datasets.

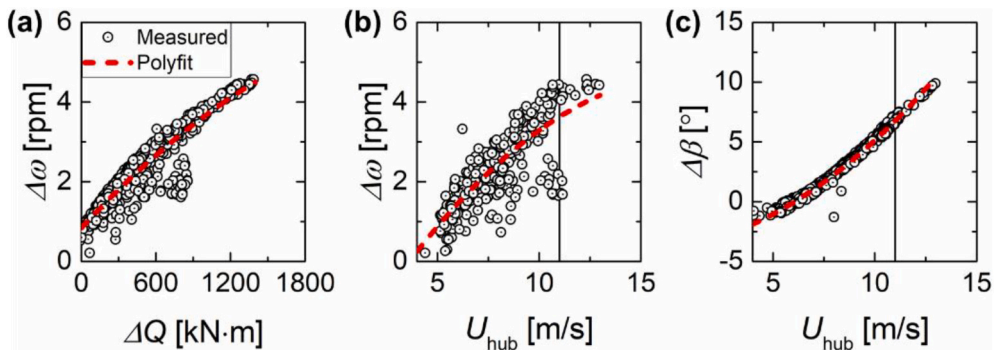


Fig. 6. The dependence of (a) rotor speed deficit ( $\Delta\omega$ ) on torque deficit ( $\Delta Q$ ), and (b) rotor speed deficit ( $\Delta\omega$ ) and (c) pitch angle deficit ( $\Delta\beta$ ) upon inflow wind speed ( $U_{hub}$ ) for the data in P2-I. Note that  $\Delta$  refers to the difference between the measured and no-icing quantities, for example,  $\Delta\omega = \omega_{no-icing} - \omega_{mea}$ .

power. However, higher deficits occur, particularly in the time periods of higher power outputs with an average deficit close to 40%. Such value is higher than the power loss (i.e.,  $\sim 35\%$ ) even after a 24-h in-cloud icing period simulated by Etemaddar et al. (2014). We attribute such discrepancy to the precipitation icing in the current study. Such an icing condition is often present in the field but has not been fully considered in most simulations. Compared with in-cloud icing conditions used in

Etemaddar et al. (2014), precipitation ice can yield a significantly higher ice accretion rate on the turbine blade and thus result in more turbine power loss in a shorter period of time. As moving to P2-T (Fig. 7c), the power loss increases as expected, but the fluctuation of measured power dampens, particularly before the transition, potentially because the blades with increasing ice accretion become less responsive to the inflow changes. The sharp drop of the measured power from  $\sim 400$  kW to zero

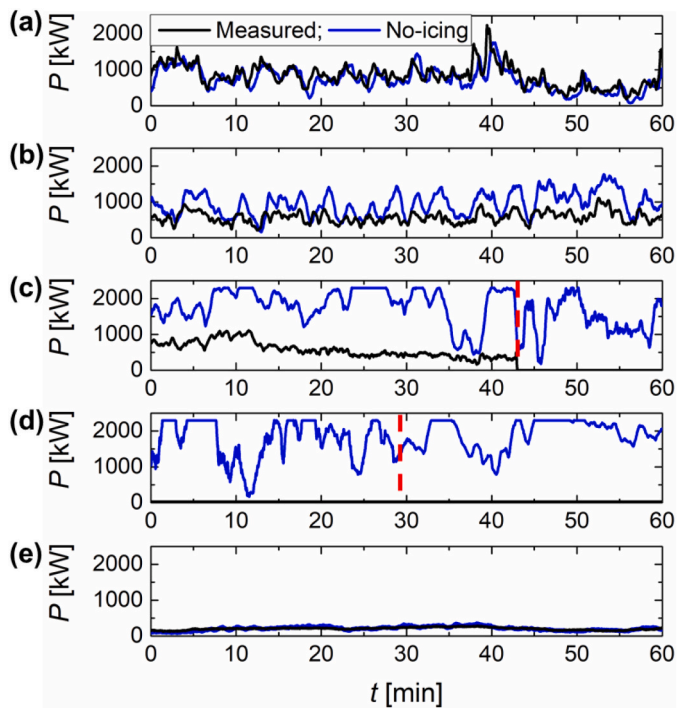


Fig. 7. Time series of the measured and no-icing power for (a) P1, (b) P2-I, (c) P2-T, (d) P3, and (e) P4 datasets.

observed at the transition indicates that the turbine alters its functional status as soon as it reaches the operational limit immediately according to the conventional control strategy. As shown in Fig. 7(d), the measured power in P3 of the stopped icing phase stays zero despite changes in the turbine operation (i.e.,  $\omega$ ,  $\beta$ ). In P4 near the end of the post-icing phase, the measured power matches well with the no-icing values with a discrepancy of only 2% due to the remaining ice accretion on blades.

Fig. 8 (a) compares the measured power in each sample datasets with the ideal power curve of the turbine. In general, the measured power outputs in P1 and P4 oscillate around the ideal curve, and P3 has no power output. The measured power in P2-I and P2-T during the operational-icing phase are highly scattered but stays mostly below the curve. In comparison to that in P2-I, the distribution of measured power in P2-T (before the transition at  $\sim 42$  min) shows a broad range of scattering corresponding to a larger fluctuation of power loss at different

wind speeds. Especially at wind speeds higher than 11 m/s, the measured power ( $P = \omega Q$ ) shows two clusters (circled in Fig. 8a) associated with the changing turbine operation (i.e.,  $\omega$  and  $\beta$ ) and torque ( $Q$ ) due to increasing blade ice accretion. The inset in Fig. 8(a) shows a strong correlation between power loss ( $\Delta P$ ) and wind speed, in which more significant  $\Delta P$  is observed at higher wind speeds. Such a trend is related to the correlation of  $\Delta\omega$  and  $\Delta\beta$  with inflow wind speed presented in Fig. 6(b) and (c). The increase of  $\Delta\omega$  and  $\Delta\beta$  can lead to blade angle of attack (AoA) exceeding its designed values at higher wind speeds, causing a stall and other aerodynamic degradation at local blade sections and thus more severe power loss.

Fig. 8 (b) shows the non-dimensional power coefficient ( $C_p = P / \frac{1}{2} \rho A U_{hub}^3$ , where  $A$  is the rotor projection area) as a function of the tip speed ratio ( $TSR = \omega R / U_{hub}$ , where  $R$  is the radius of the turbine rotor), which is widely used to assess the wind turbine performance in the literature. In P1, the measured  $C_p$  scatters below the ideal curve, and as indicated by the polynomial fitting curve of the measured dataset, the discrepancy between the measured  $C_p$  and ideal values at the corresponding TSRs is the highest at the optimal TSR of 8.3. These trends are largely due to the delay of turbine control in response to incoming flow change in practice. In P2-I and P2-T,  $C_p$  degrades substantially due to the continuous ice accretion on turbine structures. The maximum degradations of  $C_p$  observed at  $TSR_{opt}$  for P2-I and P2-T are  $\sim 20\%$  and  $\sim 30\%$  in comparison to the value in P1, respectively, as shown by the fitting curves. In P3,  $C_p$  drops to zero. In P4, the measured  $C_p$  shows a cutback due to the remaining ice on the turbine. Note that the low inflow wind speeds in P4 amplify the variations in TSR induced by the change in  $\omega$ , resulting in a wide scatter of  $C_p$ s. Noteworthy, compared with the ideal  $C_p$  curve, the measured  $C_p$  not only drops down due to the ice-induced degradation in aerodynamic properties but also shifts to lower TSRs due to the variation in turbine rotor speed associated with icing. Such icing-induced turbine rotation has not been fully considered in most simulations of turbine icing, which may lead to an over or underestimate of  $C_p$  depending on the TSR range of simulated turbine.

### 3.3. Structural degradation characterization

Following the assessment of icing impact on power reduction, the influence of icing on the structural response of turbine blades is also investigated using blade strain measurements. The flapwise blade bending moment ( $M_{Flap}$ ) and edgewise blade bending moment ( $M_{Edge}$ ) are calculated based on the differences between the strain measurements at HP and LP, and LE and TE, respectively (Gao et al., 2020b). Note that  $M_{Flap}$  and  $M_{Edge}$  are along with the directions perpendicular

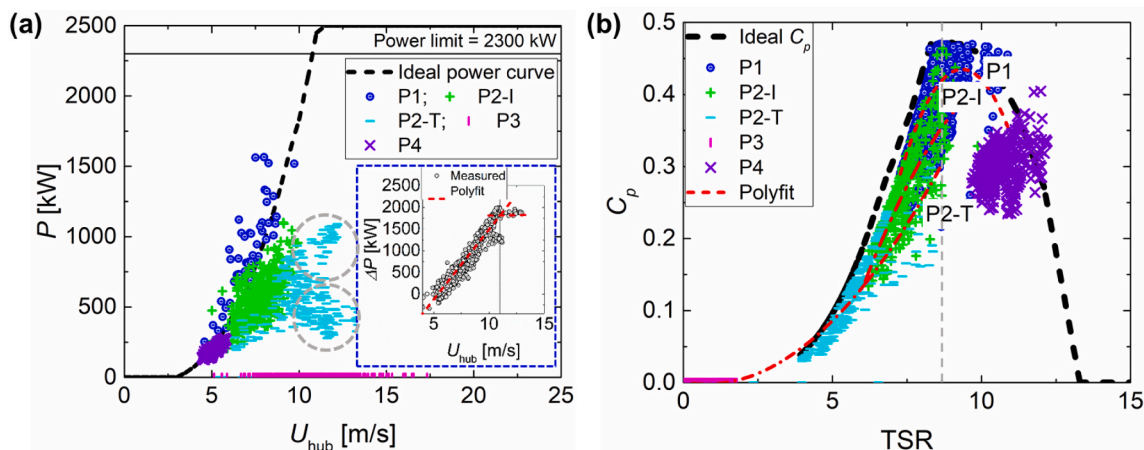


Fig. 8. (a) Power ( $P$ ) and power deficit ( $\Delta P$ , inset plot) as a function of wind speed ( $U_{hub}$ ). The gray circles mark the portion of data before (top) and after (bottom)  $\sim 12$  min in P2-T. (b) Power coefficient ( $C_p$ ) as a function of tip speed ratio (TSR). The measured data for P1, P2-I, and P2-T are least-square fit with the second-order polynomial (shown as dashed-dotted lines in the figure) for comparison with the ideal  $C_p$  curve. The gray dash line corresponds to the optimal TSR (i.e.,  $TSR_{opt}$ ).

and parallel to the chord of the blade cross-section, respectively. The moments at different radial positions of three blades show similar trends, and thus only the results at the blade root of one blade are presented in the following work to represent the icing impact on blade structural response.

Fig. 9 shows the time series of  $M_{Flap}$  and  $M_{Edge}$  for different sample datasets. In P1 of the pre-icing phase, no appreciable icing effect on  $M_{Flap}$  and  $M_{Edge}$  is observed in comparison to the blade response results under no icing but similar inflow conditions (Gao et al., 2020b). Specifically, the  $M_{Flap}$  and  $M_{Edge}$  exhibit clear periodical features corresponding to the rotor rotation frequency ( $f_r$ ), and the  $M_{Flap}$  shows a significantly higher amplitude and more jitters (comparing to  $M_{Edge}$ ) due to its higher sensitivity to the change of turbine structural configuration (i.e., the change of blade positions with respect to the turbine tower). In P2-I of the operational-icing phase, the periodic feature in the  $M_{Flap}$  signal diminishes as the aerodynamic characteristics of blade degrades upon the ice-induced changes in its cross-sectional shape (Fig. 9b). In contrast, the periodicity of  $M_{Edge}$  signal retains, and its positive and negative values indicate the moments along and against the rotational direction of the blade, which is little affected by the ice accretion (Gao et al., 2020b). However, we observe that the  $M_{Flap}/M_{Edge}$  yields a 20% decrease on average in comparison to that of the no icing case. Such

difference can be attributed to the combined effect of degraded lift and increased blade mass due to ice accretion.

As the turbine transitions to the later stage of the operational-icing phase (P2-T, shown in Fig. 9c), the periodic feature in the  $M_{Flap}$  signal also blurs due to the increasing ice accretion on turbine blades, while that in  $M_{Edge}$  is less affected, similar to the observations in P2-I. As the blades feather to  $\sim 80^\circ$  at  $\sim 42$  min of P2-T, the  $M_{Flap}$  starts to oscillate at a higher amplitude with increased periodicity while the  $M_{Edge}$  shows a significantly reduced oscillation. With more ice accretion on blade surfaces (the beginning of P3 in the stopped-icing phase), the oscillations in the  $M_{Flap}$  and  $M_{Edge}$  signals become more irregular as the blade idles around its equilibrium position (Fig. 9d). The induced blade oscillation substantially increases the magnitude of  $M_{Flap}$ , which is highly detrimental for blades and can lead to potential structural damage. As the turbine pitch reduces ( $\sim 28$  min from the start of P3), the periodicity in  $M_{Flap}$  and  $M_{Edge}$  re-emerges with a much longer cycle due to the very small  $\omega$  in this phase (no power generation). The  $M_{Flap}$  signal contains appreciable jitters, potentially corresponding to the ice-accretion caused blade loading imbalance that enhances the vibration or natural resonance of the blade at high frequencies. Near the end of the post-icing phase (P4 shown in Fig. 9e), the  $M_{Flap}$  and  $M_{Edge}$  signals present similar features to those in P1 with no appreciable icing impact

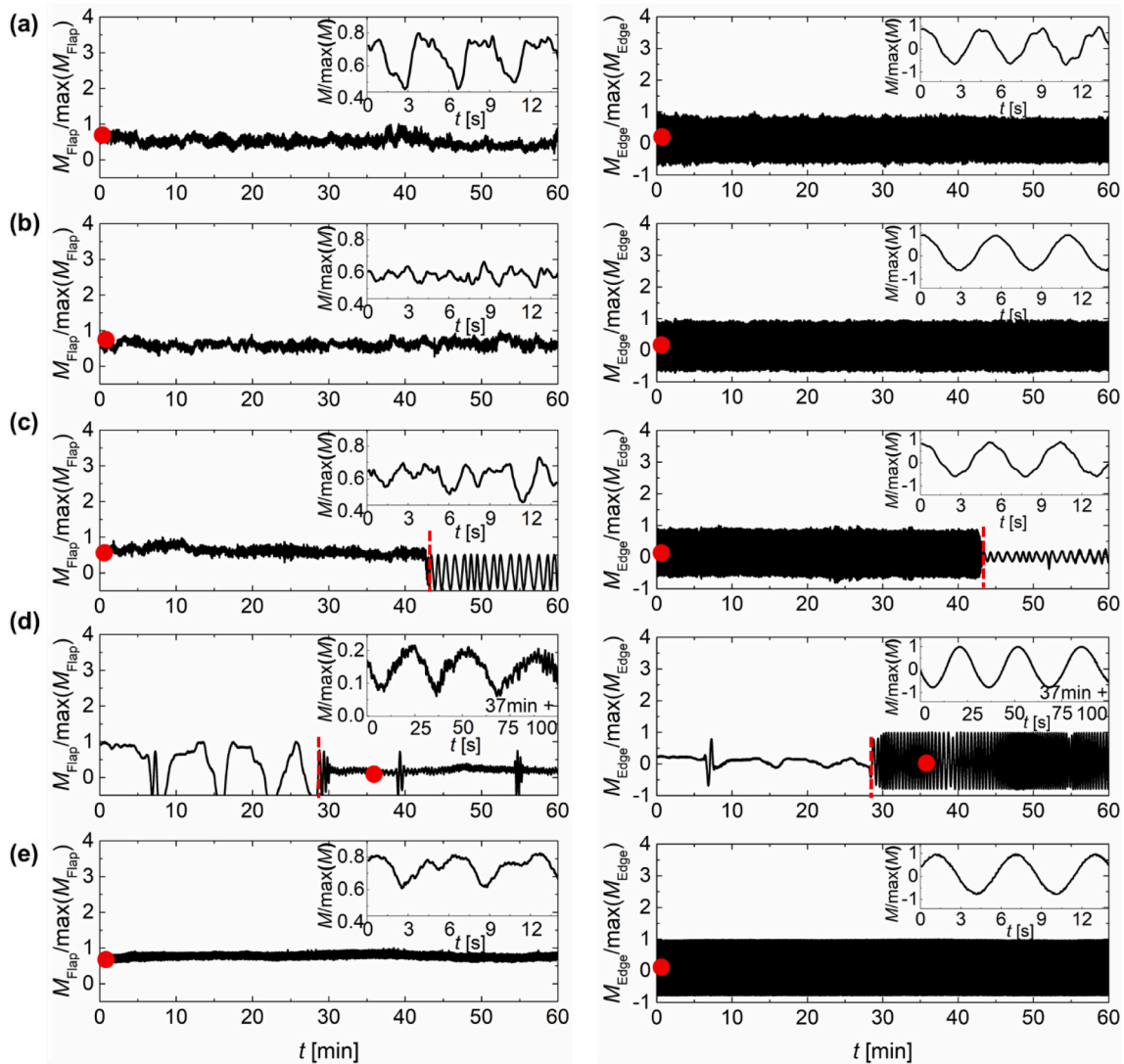


Fig. 9. Time series of the normalized flapwise blade root bending moment ( $M_{Flap}/\max(M_{Flap})$ ) and edgewise blade root bending moment ( $M_{Edge}/\max(M_{Edge})$ ) for (a) P1, (b) P2-I, (c) P2-T, (d) P3, and (e) P4 datasets. The inset figures show the normalized blade root bending moments over short periods as denoted with red dots to present more details.

observed.

To have a better understanding of the blade structural responses in each icing phase, spectral analysis for the  $M_{Flap}$  and  $M_{Edge}$  signals are conducted, as shown in Fig. 10. In P1 of the pre-icing phase, the spectra of the  $M_{Flap}$  and  $M_{Edge}$  signals show similar features to no icing case presented in the literature (Gao et al., 2020b). Specifically, the spectra of the  $M_{Flap}$  and  $M_{Edge}$  signals exhibit dominant peaks corresponding to the rotational frequency (i.e.,  $f_T = 0.2$  Hz) and its high-order harmonics. In comparison to the  $M_{Edge}$  signals, the spectrum of the  $M_{Flap}$  signal yields higher energies at  $2f_T$  and  $3f_T$  (i.e., the blade passing frequency  $f_{BPF}$ ), which explains the high-frequency jitters in the periodic time series of  $M_{Flap}$  data. Besides, the prominent spectral peaks in the higher frequency range of  $M_{Flap}$  (i.e., at 0.60 Hz and 1.9 Hz) and  $M_{Edge}$  (i.e., at 1.0 Hz and 3.1 Hz) agree well with the 1st and 2nd modes of natural blade frequencies in flapwise and edgewise directions, respectively. Remarkably, compared with no icing case (inset in Fig. 10a), the spectral peaks at  $f_T$  in the  $M_{Flap}$  and  $M_{Edge}$  signals are broadened, potentially due to the time-varying blade shapes with continuous ice accretion. This trend implies that the blade structural response is more sensitive to icing influence and can be potentially used as an effective marker for timely and accurate ice detection/identification.

In P2-I of the operational-icing phase, as shown in Fig. 10(b), the slight rotor speed reduction results in the spectral peaks in the  $M_{Flap}$  and  $M_{Edge}$  signals shifting from 0.22 Hz (no icing with same inflow conditions) to  $f_T = 0.19$  Hz. At  $f_T$ , the spectrum of the  $M_{Flap}$  yields much lower energy than that of the  $M_{Edge}$ , different from the same magnitudes observed in P1, suggesting the enhanced ice-induced effect on lift degradation. In addition, like the observation in P1, the spectral peaks at  $f_T$  are also broadened associated with the constantly-evolving ice

accretion. The natural blade frequencies remain the same values as those in P1, indicating that they are not affected by ice accretion or operation changes.

In the latter stage of the operational-icing phase, i.e., P2-T in Fig. 10 (c), the appreciable rotor speed reduction before the transition at  $\sim 42$  min leads to the spectral peaks at  $f_{T1} = 0.20$  Hz (instead of 0.25 Hz for the no icing case under same inflow conditions) in the  $M_{Flap}$  and  $M_{Edge}$  signals. At  $f_{T1}$ , the spectrum of  $M_{Flap}$  yields even lower energies than that of the  $M_{Edge}$  due to the diminished lift, similar to the observation in P2-I. In addition, the substantial decrease after the transition contributes to the spectral peaks at  $f_{T2} = 0.04$  Hz. However, at  $f_{T2}$ , an opposite trend that the spectrum of the  $M_{Flap}$  yields higher energies than that of the  $M_{Edge}$  is observed. Such a trend is primarily associated with the enhanced periodicity in the  $M_{Flap}$  signals caused by the increased contribution from gravity. The secondary reason is potentially related to the stronger correlation between the  $M_{Flap}$  and the large-scale inflow structures in the lower frequency range (i.e.,  $f < f_D$ ) in comparison to the  $M_{Edge}$ . Besides, the natural blade frequencies in flapwise and edgewise directions yield no deficits in comparison to the no icing case, suggesting that identification of turbine icing with decreased natural frequency as reported in the lab-scale experimental work (Gantasala et al., 2018) is not applicable in this icing phase.

In P3 of the stopped-icing phase, the turbine stays idling around its equilibrium position before  $\sim 28$  min and no clear spectral peaks corresponding to the rotational frequency at  $f_{T1} = 0.0036$  Hz, as shown in Fig. 10(d). In the latter period (after  $\sim 28$  min) with a reduction in pitch angle, the turbine starts slowly rotating with no power generation, contributing to the spectral peaks at  $f_{T2} = 0.04$  Hz in the  $M_{Flap}$  and  $M_{Edge}$  signals, significantly lower than 0.21 Hz in the no icing case where the

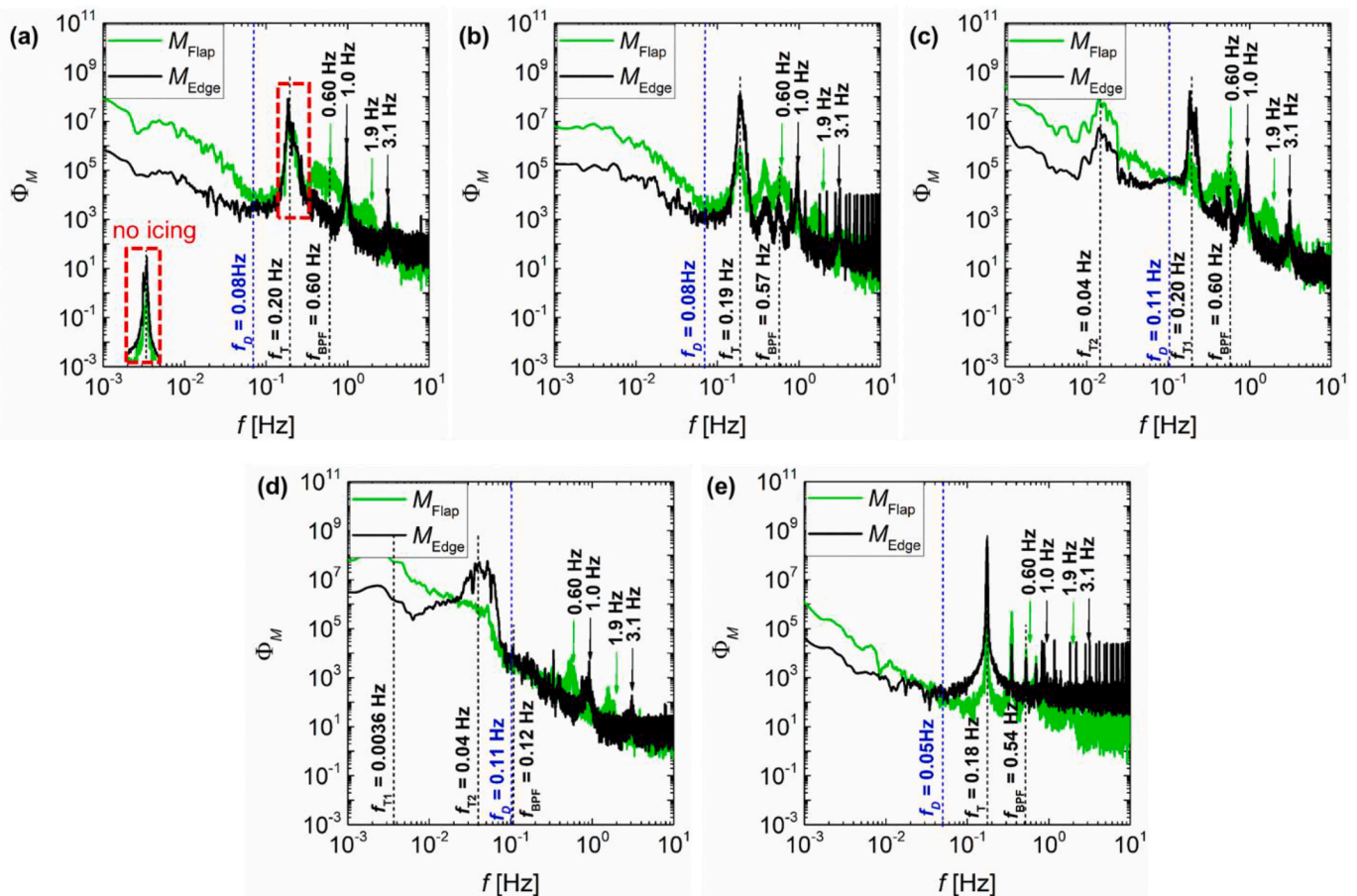


Fig. 10. Power spectra of the flapwise blade root bending moment ( $M_{Flap}$ ) and edgewise blade root bending moment ( $M_{Edge}$ ) for (a) P1, (b) P2-I, (c) P2-T, (d) P3, and (e) P4 datasets. Demarcated by the rotor frequency ( $f_D = U_{hub}/D$ ), two frequency ranges are referred to as the lower (i.e.,  $f < f_D$ ) and higher (i.e.,  $f > f_D$ ) ranges.

turbine is producing power. At  $f_{T2}$ , the spectrum of  $M_{Flap}$  yields much lower energies than that of the  $M_{Edge}$ , opposite to the observation in P2-T, mainly due to the reduced pitch angle and the substantial ice-induced lift degradation. Noticeably, the natural blade frequencies for the  $M_{Flap}$  slightly decrease while those for  $M_{Edge}$  almost stay the same as the no icing case, indicating the natural blade frequencies corresponding to the 1st and 2nd flapwise modes are more sensitive to icing effects.

In P4, the spectra of the  $M_{Flap}$  and  $M_{Edge}$  signals exhibit sharp peaks at  $f_T = 0.18$  Hz as the no icing case because the turbine almost returns to its normal operation near the end of the post-icing phase, as shown in Fig. 10(e). However, the remaining ice structures lead to an appreciable reduction in the natural blade frequencies in both flapwise and edgewise directions in comparison to the no icing case. Noteworthy, (Gantasala et al., 2018) suggested that ice-induced natural frequency deficits can be used for ice detection based on their well-controlled lab-scale experiments. However, considering the natural frequency variations in all icing phases observed in our experiments, we conclude that such natural frequency deficits are likely to be phase/flow-dependent and therefore are an effective parameter for ice detection in the field.

In addition to the blade response, the tower structural responses in terms of the fore/aft moment ( $M_{FA}$ ) and the side-to-side moment ( $M_{SS}$ ) are also investigated for each icing phase. The pairs of the strain measurements along and perpendicular to the inflow wind direction are used to estimate the  $M_{FA}$  and  $M_{SS}$ , respectively. Note that the time sequences of the  $M_{FA}$  and  $M_{SS}$  are not presented in the current study since their signals are strongly correlated with inflow speed and exhibit no appreciable signatures related to icing.

Fig. 11 presents the power spectra of the  $M_{FA}$  and  $M_{SS}$  signals for different icing phases. In P1 of the pre-icing phase, as shown in Fig. 11 (a), the spectra of the  $M_{FA}$  and  $M_{SS}$  signals present similar signatures to

the no icing case reported in the literature (Gao et al., 2020b). Specifically, the spectra of the  $M_{FA}$  and  $M_{SS}$  show dominant peaks at  $3f_T$  (i.e., the blade passing frequency  $f_{BPF}$ ) rather than  $f_T$  in blade response spectra. In comparison to the  $M_{SS}$ , the spectrum of the  $M_{FA}$  signals yields higher energies at  $f_T$  since it is more sensitive to the rotation imbalance induced by the wind shear effect within a rotational cycle. The spectral peaks observed at 0.33 Hz match well with the natural frequency of the 1st tower mode for the no icing turbine.

In P2-I of the operational-icing phase, as shown in Fig. 11(b), the reduction in rotor speed leads to the spectral peaks of the  $M_{FA}$  and  $M_{SS}$  signals shifting to slightly lower frequencies (i.e., at  $f_T = 0.19$  Hz and  $f_{BPF} = 0.57$  Hz vs. 0.22 Hz and 0.66 Hz for no icing case under the same inflow conditions). The rotor speed reduction also results in the overall lower energies observed in the spectrum of the  $M_{SS}$  signals than that of the  $M_{FA}$ , since the  $M_{FA}$  signals are less sensitive to the rotor speed reduction. Besides, different from the observations in P1, the energy levels of the spectral peaks at  $f_T$  in the  $M_{FA}$  and  $M_{SS}$  signals increase to the comparable levels to the peaks at  $f_{BPF}$ , suggesting the increasing rotation imbalance due to ice accretion. Furthermore, the spectra of  $M_{FA}$  and  $M_{SS}$  signals exhibit much higher energies at the natural frequency of 0.33 Hz associated with its enhanced sensitivity to the wind shear with ice accretion.

The P2-T of the latter stage of the operational-icing phase exhibit generally similar trends to those in P2-I, as shown in Fig. 11(c). Specifically, the spectral peaks of the  $M_{FA}$  and  $M_{SS}$  signals at  $f_T$  and  $f_{BPF}$  shift from 0.25 Hz and 0.75 Hz (no icing case) to the lower frequencies of 0.20 Hz and 0.60 Hz associated with the rotor speed reduction before the transition at  $\sim 42$  min. The spectral peaks corresponding to the natural frequency of the 1st tower mode remain at 0.33 Hz with high energy levels. The spectrum of the  $M_{SS}$  signals yields overall lower energies than

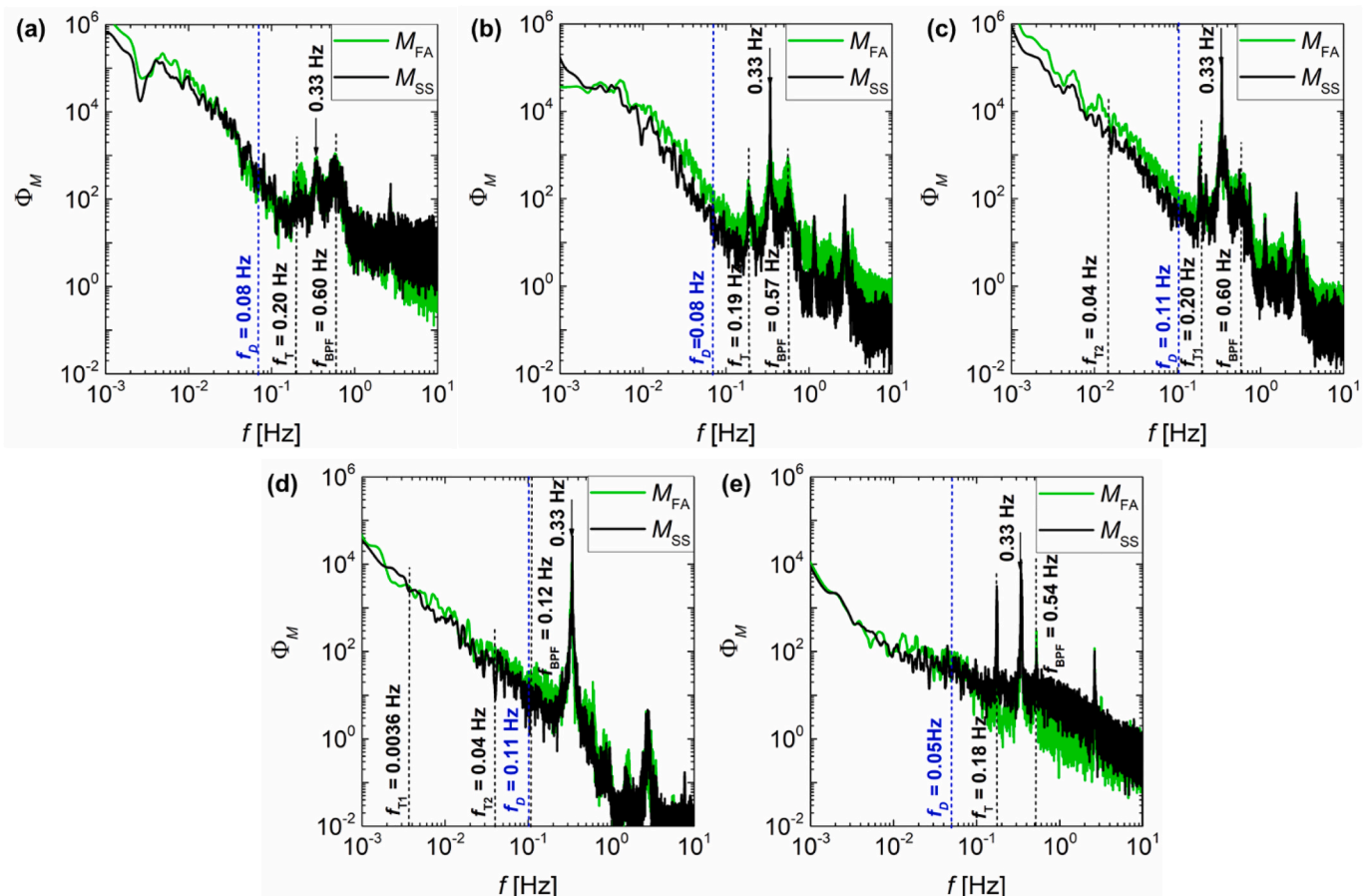


Fig. 11. Power spectra of the tower fore/aft moment ( $M_{FA}$ ) and side-to-side moment ( $M_{SS}$ ) for (a) P1, (b) P2-I, (c) P2-T, (d) P3, and (e) P4 datasets.

that of the  $M_{FA}$  signals. However, in contrast to the observations in P1 and P2-I, the spectral peaks at  $f_T$  exhibit higher energies in comparison to the peaks at  $f_{BPF}$  associated with the enhanced rotation imbalance. In addition, unlike the blade response, no clear peaks in the spectra of the  $M_{FA}$  and  $M_{SS}$  signals correspond to the blade rotation after the transition, suggesting that the slow rotation has a limited effect on the turbine-scale structural behaviors.

In P3, the turbine comes into the stopped-icing phase with no power generation and substantial rotor speed reduction. In comparison to the blade spectra, the spectra of  $M_{FA}$  and  $M_{SS}$  signals present no clear peaks at  $f_T$  and  $f_{BPF}$  in spite of the significant change of blade pitch (i.e., blade pitches to small magnitude from its featuring of  $\sim 80$  after  $\sim 28$  min), indicating these signals are insensitive to the blade operation during this phase. In comparison to P2-T (the similar inflow conditions, i.e., Region 2.5), the spectra of the  $M_{FA}$  and  $M_{SS}$  signals show much lower energies due to the substantially reduced rotor speed. In addition, the natural frequency of 1st tower mode remains at 0.33 Hz, which is not affected by ice accretion or turbine operation.

As the turbine almost returns to its normal operation in P4 near the end of the post-icing phase, as shown in Fig. 11(e), the spectral peaks re-emerge at  $f_T$  and  $f_{BPF}$  in the  $M_{FA}$  and  $M_{SS}$  signals. The spectra of  $M_{FA}$  and  $M_{SS}$  signals exhibit higher energy levels at  $f_T$  than those at  $f_{BPF}$  associated with the strong effect of the rotational imbalance, potentially due to the remaining ice and occasional ice shedding. It should be noted that the overall lower energies observed in the spectra of the  $M_{FA}$  and  $M_{SS}$  signals are mainly related to the small inflow wind speeds (Region 1.5). The natural frequency of the 1st tower mode retains the same as its original value for no icing turbine. In summary, the icing event has a negligible effect on natural tower frequency.

To have a better understanding of the ice-induced loading imbalance, the strain distribution at the tower base is analyzed for each icing phase using the normalized strain measurements ( $\epsilon/\epsilon_{max}$ , where  $\epsilon_{max} = (\max(\epsilon) + |\min(\epsilon)|)/2$ ), as shown in Fig. 12. The 0-axis for each sub-figure is set to be along with the inflow direction. In addition, the symmetry index (defined as  $SI = \sum |\epsilon_{side1} - \epsilon_{side2}| / (n\epsilon_{max}) \times 100\%$ , where  $\epsilon_{side1}$  and  $\epsilon_{side2}$  are the strain measurements on two sides of the axis of symmetry (i.e., 0–180 axis highlighted with red lines in Fig. 12);  $n$  is the number of pairs of strain measurements,  $n = 10$  in the present study) is used to quantify of the asymmetry of the strain distribution and thereby reflect the potential loading imbalance.

In P1 of the pre-icing phase, as shown in Fig. 12(a), the strain distribution shows similar symmetric signatures to the no icing case presented in the literature (Chamorro et al., 2015b). Specifically, the positive and negative values refer to tension and compression, respectively. The absolute magnitude of strain reaches the maximum along with the inflow wind direction corresponding to the prevailing wind-driven  $M_{FA}$ . The rotor rotation leads to a slight asymmetry of  $SI = 13\%$  related to the  $M_{SS}$ . As the turbine moves from P2-I (Fig. 12b) to P2-T (Fig. 12c) of the operational-icing phase, the  $SI$  exhibits a significant increase of asymmetry from 17% to 34% (Fig. 12f), potentially due to the increasing ice accretion and caused loading imbalance of the turbine structure. As the turbine enters the standstill/idling status in P3 (Fig. 12d), the asymmetry of the loading shows little change (i.e., stays around  $SI$  of 34%). In P4 near the end of the post-icing phase, the remaining ice on the turbine generates no power deficits, but it has a significant impact on the loading imbalance reflected by the  $SI = 26\%$ . This observation also resonates with the higher energy levels of the spectral peaks at  $f_T$  than those at  $f_{BPF}$  of the  $M_{FA}$  and  $M_{SS}$  signals shown in

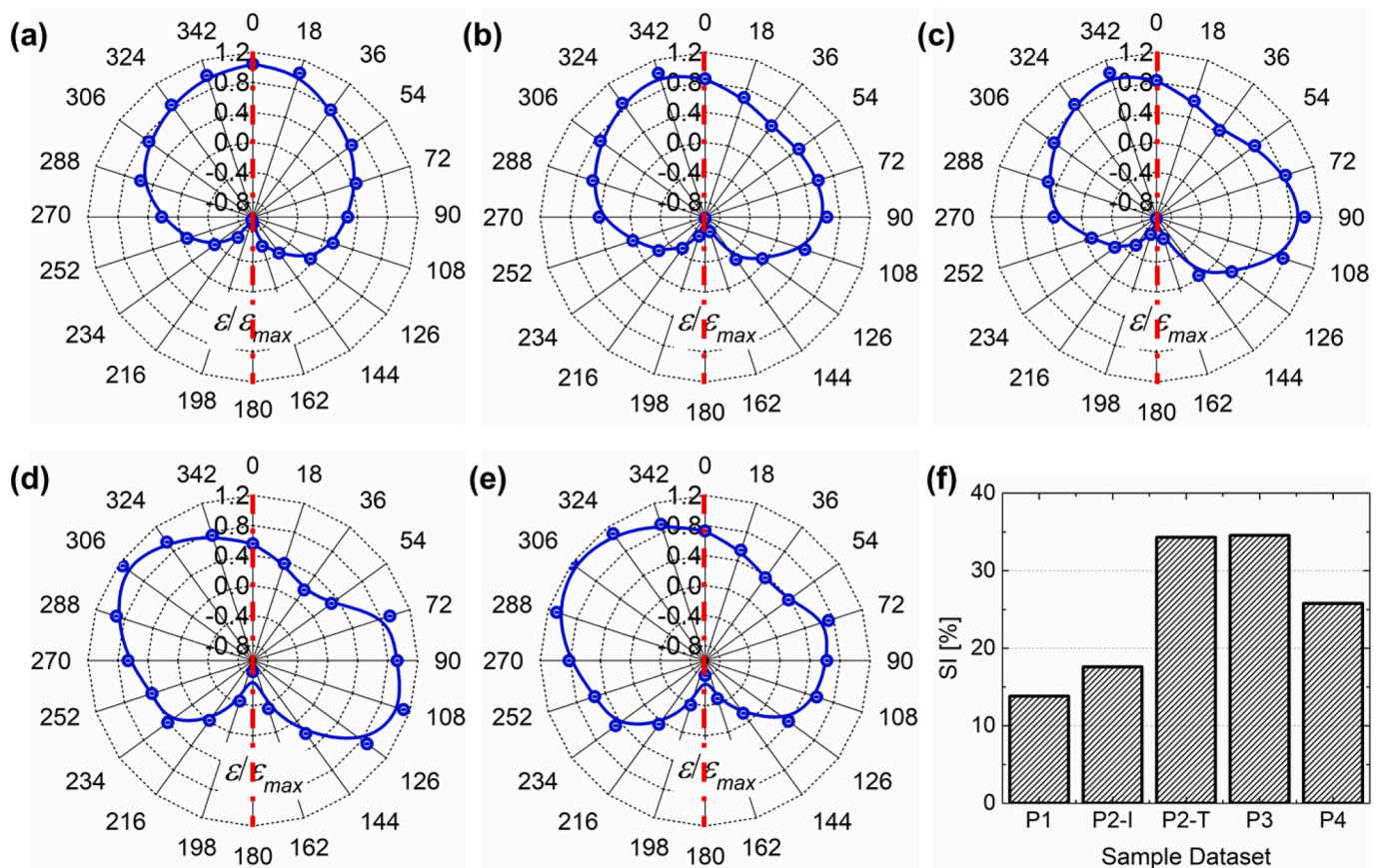


Fig. 12. Tower strain distribution ( $\epsilon/\epsilon_{max}$ ) at tower base for (a) P1, (b) P2-I, (c) P2-T, (d) P3, (e) P4 datasets, and (f) the symmetry index (SI) to characterize the distribution asymmetry. The maximum strain magnitude normalizes the tower strain measurements,  $\epsilon_{max} = (\max(\epsilon) + |\min(\epsilon)|)/2$ , where  $\epsilon$  is the set of strain readings from all 20 strain gauges at a single timestamp. The red lines in (a-e) correspond to the axis of symmetry.

Fig. 11(e).

#### 4. Conclusions and discussions

The current study presents a systematic characterization of the performance degradation of a utility-scale wind turbine under natural icing environments using the field database from the Eolos Wind Energy Research Station (belongs to the IEA Ice Class 2 area). The database contains the meteorological icing (temperature and relative humidity) and flow conditions, wind turbine operation conditions, blade and tower strain measurements, and the supporting photos of ice-accreted turbine blades. A representative icing event that lasts 51 h is selected and divided into the pre-icing, operational-icing, stopped-icing, and post-icing phases, mainly based on the variations of turbine operational conditions in terms of power output, rotor speed, and pitch angle. For each icing phase, a 1-h sample datasets are selected to provide a detailed evaluation of the ice-induced effect on turbine operation, power production, and structural response. The main findings are summarized as follows.

There is no detectable icing impact on turbine operation in the pre-icing phase, even if the meteorological conditions are satisfied. The appreciable reductions in the rotor speed and pitch angle (i.e., the differences between the measured values under icing conditions and modeled values under no icing conditions with same inflow speeds) declare the onset of the operational icing phase. Such reductions are found to enlarge as the inflow wind speed increases, which may accelerate the blade/airfoil stall process and contribute to more severe power deficits. With the increasing ice accretion, the turbine reaches its operational limit and enters the stopped-icing phase, where the pitch angle dramatically increases to its feathering value (may not exactly  $90^\circ$  in the field), and the rotor speed drops to almost zero. In this period, the turbine produces no power even if the pitch angle may reduce with a slight increase of the rotor speed due to the occasional ice shedding from the turbine blades. As the turbine restarts to generate power, the post-icing phase begins. The power deficit gradually diminishes as the ice melts and becomes negligible near the end of this phase, during which the deficit in the rotor speed remains appreciable, potentially due to the small amount of residual ice on the turbine structures.

During the 51-h icing event, the turbine has a total energy loss of approximately 25 MWh, i.e., 63% of the amount of energy to be generated ( $\sim 40$  MWh). For a 0.10  $\$/kWh$  contract, this energy loss is equivalent to a  $\$ 2511$  financial deficit for this event. Following the stopped-icing phase (71%), the post-icing phase yields the second-largest share of the energy loss (17%) due to its long duration associated with slow natural ice melting while the operational-icing phase contributes to a share of 12%. It should be noted that at the end of the operational-icing phase, the turbine power exhibits a sudden drop from  $\sim 400$  kW to zero rather than a smooth transition when the turbine reaches its operational limit based on the conventional control strategy. In addition, the power deficit shows a strong correlation with the inflow speed associated with the aforementioned more substantial decreases of rotor speed and pitch angle at higher wind speeds. The non-dimensional power coefficient ( $C_p$ ) vs. tip speed ratio (TSR) curve shows a strong dependence of the  $C_p$  deficits with respect to the changes in TSR (i.e., decrease in value due to ice) during the turbine operating in icing environments, which has not been considered in most of the blade icing simulations nowadays due to the difficulty in coupling the icing process and turbine operation changes. The result shows the  $C_p$  reaches its maximum degradation around the optimal TSR ( $TSR_{opt} = 8.3$ ) of the turbine.

The blade structural response is found to be highly sensitive to the icing effect. The potential ice accretion in the pre-icing phase causes the broadening of the spectral peaks of the blade signals due to their fast reactions to the lift penalties associated with the blade leading-edge ice accretion. In the operational-icing phase, the periodicity in the flapwise blade root bending moment ( $M_{Flap}$ ) substantially blurs as the

aerodynamic characteristics of blades degrade further upon the ice-induced changes in its cross-sectional shape. In contrast, the periodicity of edgewise moment ( $M_{Edge}$ ) retains because it is dominated by the gravitational force of the turbine blade, which is not significantly affected by the ice accretion (Gao et al., 2020b). As the turbine blade feather during the transition to the subsequent stopped-icing phase, the ice-induced blade oscillation substantially increases the magnitude of  $M_{Flap}$ , which is highly detrimental for blades and can lead to potential structural damage. The natural frequencies corresponding to the 1st and 2nd blade flapwise modes slightly decrease in this period while those for edgewise modes remain the same as the no icing case. In the post-icing phase, the natural frequencies in both flapwise and edgewise directions present an appreciable reduction.

In comparison to the blade structural response, the tower structural response is less influenced by the ice-induced rotor speed variation. If the rotor speed drops below the rotor frequency (i.e.,  $f_D = U_{hub}/D$ , where  $U_{hub}$  and  $D$  refer to the hub-height wind speed and the rotor diameter), the tower structural signals yield no spectral peaks corresponding to the rotor rotation. The natural frequency corresponding to the 1st tower mode remains the same as the no icing case across all icing phases. However, the dominant spectral peaks observed in the tower fore/aft and side-to-side moments ( $M_{FA}$  and  $M_{SS}$ ) at the blade passing frequency ( $f_{BPF} = 3f_T$ ) for the no icing case are overshadowed by the spectral peaks corresponding to the rotational frequency ( $f_T$ ) due to the ice-induced loading imbalance. With the strain distribution at the tower base, a significant increase in asymmetry from 13% (pre-icing phase) to 34% (stopped-icing phase) presents the enhanced loading imbalance in the course of the icing event. Even with a small amount of remaining ice near the end of the post-icing phase, the strain distribution also yields an asymmetry of 26%, indicating that the ice-induced loading imbalance is substantial for the turbine operating in the field.

Our findings not only bring insights into the improvements for the conventional ice detection techniques but also inspire the development of novel ice detection approaches, particularly for the indirect methods based on the good understandings of how the turbine behaves during an icing event (Dao et al., 2018; Zhang et al., 2018). The indirect methods, unlike the direct methods, require no installation of ice sensors or on-board cameras and thus are highly flexible, cost-competitive, and demanded in the market. Based on our findings, the blade structural response (the broadening of the spectral peaks of the blade signals) is the most sensitive indicator for the icing effect due to its fast reaction to the ice-induced lift penalties at the early stages of an icing event, i.e., pre-icing and operational-icing phases. If the conditions permit, blade strain measurement is highly recommended for the turbines in cold climate regions. The strain response performs in a similar function as the ice detection sensors based on different types of accelerometers, such as BLADEcontrol (Bosch Rexroth), Fos4X, and Wölfel IDD.Blade (Cattin and Heikkilä, 2016), and it might be more susceptible to the influence of noises. Interestingly, our finding that the changes of the blade natural frequencies are not detectable in the early stages of an icing event, i.e., pre-icing and operational-icing phases. Such information implies that the methods based on the variations in the natural blade frequencies used in Fos4X and BLADEcontrol (Bosch Rexroth) may not be that sensitive for ice detection at early stages. More investigations are needed for a more detailed and quantitative comparison. For the majority of turbines not equipped with blade strain gauges, the reductions in the rotor speed and pitch angle are also more effective indicators for icing event detection than the commonly used power deficit. Furthermore, nowadays, many turbines manufacturers (e.g., GE Energy, Vestas, Enercon) offer ice protection systems (IPS) that tend to mitigate the impact of ice on the turbine behavior. The best operational strategy for IPS is still an open-ended question in the community as it depends on a lot of meteorological (temperature, wind speed, LWC) and technological (the type of system, the power consumed, and so forth) factors. The first-hand information of the turbine behaviors in different icing phases provides inspirations for perpetuating efficient use of the current

thermal-based IPSs. For example, the onset of the post-icing phase might be a good turn-on time of the conventional thermal systems (e.g., hot air projection or resistive heating) to remove the ice structures accreted on turbine blades. Their functions are to significantly shorten the slow natural melting process and thus reduce power loss. More importantly, our findings provide a basis for the advanced control frameworks based on the different operations in various phases to compensate for the aerodynamic penalties and structural imbalance. The active pitch control and the operational stop (or active rotor speed reduction) approaches are suggested to be implemented in the pre-icing and operational-icing phases to reduce the amount of ice accreted on the turbine blades, especially over the suction-side surfaces. A lower feathering angle of the blade can trigger a positive influence on the load mitigation in the stopped-icing phase.

It should be noted that the derived findings (qualitative trends) of the present study can be generalized for variable-speed variable-pitch (VSWP) turbines operating in Regions 1.5–2.5. The different characteristics in Region 3 may influence our findings in their implementations to some extent. It also should be cautioned that more analysis of the turbine behaviors under different icing conditions (e.g., in-cloud, precipitation-icing, frost, etc.) are needed before further generalization. Future work will focus on seeking the quantitative linkage between the variations in wind turbine quantities and the amount of ice accretion for refining the advanced control frameworks mentioned above.

#### Declaration of Competing Interest

The authors declare that there is no conflict of interest regarding the publication of this paper.

#### Acknowledgments

This work was supported by the National Science Foundation CAREER Award (NSF-CBET-1454259), Xcel Energy through the Renewable Development Fund (grant RD4-13), IonE of University of Minnesota, as well as Renewable Energy Commercialization Fellowship. The authors would thank the engineers from St. Anthony Falls Laboratory, including Christopher Milliren, Chris Feist, and Matthew Lueker, for the fruitful discussion regarding the Eolos database.

#### References

- Alsabagh, A.S.Y., Tiu, W., Xu, Y., Virk, M.S., 2013. A review of the effects of ice accretion on the structural behavior of wind turbines. *Wind Eng.* 37, 59–70. <https://doi.org/10.1260/0309-524X.37.1.59>.
- Barker, A., Timco, G., Gravesen, H., Vølund, P., 2005. Ice loading on Danish wind turbines. Part 1: dynamic model tests. *Cold Reg. Sci. Technol.* 41, 1–23. <https://doi.org/10.1016/j.coldregions.2004.05.002>.
- Battisti, Lorenzo, 2015. Wind Turbines in Cold Climates: Icing Impacts and Mitigation Systems. <https://doi.org/10.1007/978-3-319-05191-8>.
- Beaugendre, H., Morency, F., Habashi, W.G., 2003. FENSAP-ICE's three-dimensional in-flight ice accretion module: ICE3D. *J. Aircr.* 40, 239–247. <https://doi.org/10.2514/2.3113>.
- Blasco, P., Palacios, J., Schmitz, S., 2017a. Effect of icing roughness on wind turbine power production. *Wind Energy* 20, 601–617. <https://doi.org/10.1002/we.2026>.
- Bragg, M.B., Broeren, A.P., Blumenthal, L.A., 2005. Iced-airfoil aerodynamics. *Prog. Aerosp. Sci.* 41, 323–362. <https://doi.org/10.1016/j.paerosci.2005.07.001>.
- Cattin, R., Heikkilä, U., et al., 2016. Evaluation of ice detection systems for wind turbines. In: VGB Research Project No. 392. Meteoest, Bern.
- Chamorro, L.P., Hong, J., Gangodagamage, C., 2015a. On the scale-to-scale coupling between a full-scale wind turbine and turbulence. *J. Turbul.* 16, 617–632. <https://doi.org/10.1080/14685248.2015.1021472>.
- Chamorro, L., Lee, S.-J., Olsen, D., Milliren, C., Marr, J., Arndt, R.E., Sotiropoulos, F., 2015b. Turbulence effects on a full-scale 2.5 MW horizontal-axis wind turbine under neutrally stratified conditions. *Wind Energy* 18, 339–349. <https://doi.org/10.1002/we.1700>.
- Dao, P.B., Staszewski, W.J., Barszcz, T., Uhl, T., 2018. Condition monitoring and fault detection in wind turbines based on cointegration analysis of SCADA data. *Renew. Energy* 116, 107–122. <https://doi.org/10.1016/j.renene.2017.06.089>.
- Davis, N.N., 2014. Icing Impacts on Wind Energy Production. DTU Wind Energy.
- Davis, N.N., Pinson, P., Hahmann, A.N., 2016a. Identifying and characterizing the impact of turbine icing on wind farm power generation. *Wind Energy* 19, 1503–1518. <https://doi.org/10.1002/we>.
- Davis, N.N., Byrkedal, Ø., Hahmann, A.N., Clausen, N.-E., Žagar, M., 2016b. Ice detection on wind turbines using the observed power curve. *Wind Energy* 19, 999–1010. <https://doi.org/10.1002/we.1878>.
- Ememaddar, M., Hansen, M.O.L., Moan, T., 2014. Wind turbine aerodynamic response under atmospheric icing conditions. *Wind Energy* 17, 241–265. <https://doi.org/10.1002/we.1573>.
- Fakorede, O., Feger, Z., Ibrahim, H., Ilincă, A., Perron, J., Masson, C., 2016. Ice protection systems for wind turbines in cold climate: characteristics, comparisons and analysis. *Renew. Sust. Energy. Rev.* 65, 662–675. <https://doi.org/10.1016/j.rser.2016.06.080>.
- Gantasala, S., Luneno, J.C., Aidanpää, J.O., 2018. Identification of ice mass accumulated on wind turbine blades using its natural frequencies. *Wind Eng.* 42, 66–84. <https://doi.org/10.1177/0309524X17723207>.
- Gantasala, S., Tabatabaei, N., Cervantes, M., Aidanpää, J.O., 2019. Numerical investigation of the aeroelastic behavior of a wind turbine with iced blades. *Energies* 12, 1–24. <https://doi.org/10.3390/en12122422>.
- Gao, L., 2019. Experimental Investigations on Wind Turbine Icing Physics and Anti-/De-icing Technology. Iowa State University.
- Gao, L., Liu, Y., Ma, L., Hu, H., 2019a. A hybrid strategy combining minimized leading-edge electric-heating and superhydro-/ice-phobic surface coating for wind turbine icing mitigation. *Renew. Energy* 140, 943–956. <https://doi.org/10.1016/j.renene.2019.03.112>.
- Gao, L., Liu, Y., Zhou, W., Hu, H., 2019b. An experimental study on the aerodynamic performance degradation of a wind turbine blade model induced by ice accretion process. *Renew. Energy* 133, 663–675. <https://doi.org/10.1016/j.renene.2018.10.032>.
- Gao, L., Veerakumar, R., Liu, Y., Hu, H., 2019c. Quantification of the 3D shapes of the ice structures accreted on a wind turbine airfoil model. *J. Vis.* <https://doi.org/10.1007/s12650-019-00567-4>.
- Gao, L., Liu, Y., Hu, H., 2020a. An experimental investigation on the dynamic glaze ice accretion process over a wind turbine airfoil surface. *Int. J. Heat Mass Transf.* 149, 119120 <https://doi.org/10.1016/j.ijheatmasstransfer.2019.119120>.
- Gao, L., Yang, S., Abraham, A., Hong, J., 2020b. Effects of inflow turbulence on structural deformation of wind turbine blades. *J. Wind Eng. Ind. Aerodyn.* 199, 104137. <https://doi.org/10.1016/j.jweia.2020.104137>.
- Gravesen, H., Sørensen, S.L., Vølund, P., Barker, A., Timco, G., 2005. Ice loading on Danish wind turbines: part 2. Analyses of dynamic model test results. *Cold Reg. Sci. Technol.* 41, 25–47. <https://doi.org/10.1016/j.coldregions.2004.05.009>.
- Hansson, J., Lindvall, J., Byrkedal, Ø., 2016. Quantification of Icing Losses in Wind Farms.
- Hendrikse, H., Ziemer, G., Owen, C.C., 2018. Experimental validation of a model for prediction of dynamic ice-structure interaction. *Cold Reg. Sci. Technol.* 151, 345–358. <https://doi.org/10.1016/j.coldregions.2018.04.003>.
- Homola, M.C., Wallenius, T., Nicklasson, Per J., Sundsbø, Per A., 2010. The relationship between chord length and rime icing on wind turbines. *Wind Energy* 13, 627–632. <https://doi.org/10.1002/we.383>.
- Homola, M.C., Virk, M.S., Nicklasson, P.J., Sundsbø, P.A., 2012a. Performance losses due to ice accretion for a 5 MW wind turbine. *Wind Energy* 15, 379–389. <https://doi.org/10.1002/we.477>.
- Homola, Matthew C., Virk, Muhammad S., Nicklasson, Per J., Sundsbø, Per A., 2012b. Performance losses due to ice accretion for a 5MW wind turbine. *Wind Energy* 15, 379–389. <https://doi.org/10.1002/we>.
- Hu, L., Zhu, X., Hu, C., Chen, J., Du, Z., 2017. Wind turbines ice distribution and load response under icing conditions. *Renew. Energy* 113, 608–619. <https://doi.org/10.1016/j.renene.2017.05.059>.
- Ihls, J., 2015. Implementation of Machine Learning to Model Losses from Icing of Wind Turbines Losses from Icing of Wind Turbines. KTH Royal Institute of Technology.
- Jasinski, W.J., Noe, S.C., Selig, M.S., Bragg, M.B., 1997. Wind turbine performance under icing conditions. In: 35th Aerosp. Sci. Meet. Exhib., 120, pp. 0–5. <https://doi.org/10.2514/6.1997-977>.
- Kraj, A.G., Bibeau, E.L., 2010. Phases of icing on wind turbine blades characterized by ice accumulation. *Renew. Energy* 35, 966–972. <https://doi.org/10.1016/j.renene.2009.09.013>.
- Laakso, T., Baring-Gould, I., Durstewitz, M., Horbaly, R., Lacroix, A., Peltola, E., Ronsten, G., Tallhaug, L., Wallenius, T., 2005. State-of-the-art of Wind Energy in Cold Climates.
- Lamraoui, F., Fortin, G., Benoit, R., Perron, J., Masson, C., 2014. Atmospheric icing impact on wind turbine production. *Cold Reg. Sci. Technol.* 100, 36–49. <https://doi.org/10.1016/j.coldregions.2013.12.008>.
- Lehtomäki, V., 2016. Wind Energy in Cold Climates Available Technologies - Report.
- Makkonen, L., Laakso, T., Marjaniemi, M., Finstad, K.J., 2001. Modelling and prevention of ice accretion on wind turbines. *Wind Eng.* 25, 3–21. <https://doi.org/10.1260/0309524011495791>.
- Molina, E.S., Silva, D.M., Righi, M., Alonso, J.J., Sa, E., José, S., 2018. Application of DDES to Iced Airfoil in SU2 Session. Springer International Publishing. <https://doi.org/10.1007/978-3-030-27607-2>.
- Morgan, Colin, Bossany, E., Seifert, H., 1998. Assessment of safety risks arising from wind turbine icing. In: Boreas VI - Wind Energy Prod. Cold Clim, pp. 113–121.
- Pedersen, M.C., Sørensen, H., 2016. Towards a CFD Model for Prediction of Wind Turbine Power Losses Due to Icing in Cold Climate, pp. 1–6.
- Reid, T., Baruzzi, G., Ozcer, I., Switchenko, D., Habashi, W.G., 2013. FENSAP-ICE simulation of icing on wind turbine blades, part 1: performance degradation. In: 51st AIAA Aerosp. Sci. Meet. Incl. New Horizons Forum Aerosp. Expo. 2013, pp. 1–18. <https://doi.org/10.2514/6.2013-750>.
- René, C., Markus, R., Gabriela, R., 2009. Four years of monitoring a wind turbine under icing conditions. In: 13th Int. Work. Atmos. Icing Struct. (IWAIS XIII), pp. 6–10.

- Ribeiro, C., Beckford, T., 2016. Icing Losses - What Can We Learn from Production and Meteorological Data?, pp. 1–10.
- Roberge, P., Lemay, J., Ruel, J., Bégin-Drolet, A., 2019. Field analysis, modeling and characterization of wind turbine hot air ice protection systems. *Cold Reg. Sci. Technol.* 163, 19–26. <https://doi.org/10.1016/j.coldregions.2019.04.001>.
- Shi, W., Tan, X., Gao, Z., Moan, T., 2016. Numerical study of ice-induced loads and responses of a monopile-type offshore wind turbine in parked and operating conditions. *Cold Reg. Sci. Technol.* 123, 121–139. <https://doi.org/10.1016/j.coldregions.2015.12.007>.
- Shu, L., Liang, J., Hu, Q., Jiang, X., Ren, X., Qiu, G., 2017. Study on small wind turbine icing and its performance. *Cold Reg. Sci. Technol.* 134, 11–19. <https://doi.org/10.1016/j.coldregions.2016.11.004>.
- Shu, L., Li, H., Hu, Q., Jiang, X., Qiu, G., McClure, G., Yang, H., 2018. Study of ice accretion feature and power characteristics of wind turbines at natural icing environment. *Cold Reg. Sci. Technol.* 147, 45–54. <https://doi.org/10.1016/j.coldregions.2018.01.006>.
- Siemens Gamesa Renewable Energy, 2019. Technology Retrofit and Service Approach for Performance. Siemens Gamesa Renewable Energy.
- Son, C., Koss, H., Kim, T., 2019. Development of Three-dimensional Icing Simulation Code for Wind Turbines, pp. 1–8.
- Tagawa, G.B.S., Morency, F., Beaugendre, H., 2018. CFD study of airfoil lift reduction caused by ice roughness. In: 2018 Appl. Aerodyn. Conf. <https://doi.org/10.2514/6.2018-3010>.
- Yirtici, O., Tuncer, I.H., Ozgen, S., 2016. Ice accretion prediction on wind turbines and consequent power losses. *J. Phys. Conf. Ser.* 753, 022022 <https://doi.org/10.1088/1742-6596/753/2/022022>.
- Zanon, A., De Gennaro, M., Kühnelt, H., 2018. Wind energy harnessing of the NREL 5 MW reference wind turbine in icing conditions under different operational strategies. *Renew. Energy* 115, 760–772. <https://doi.org/10.1016/j.renene.2017.08.076>.
- Zhang, L., Liu, K., Wang, Y., Omariba, Z.B., 2018. Ice detection model of wind turbine blades based on random forest classifier. *Energies* 11. <https://doi.org/10.3390/en11102548>.